CHAPTER FIVE

Nonattracting chaotic sets

We have already encountered situations where chaotic motion was nonattracting. For example, the map Eq. (3.3) had an invariant Cantor set in [0, 1], but all initial conditions except for a set of Lebesgue measure zero eventually leave the interval [0, 1] and then approach $x = \pm\infty$. Similarly, the horseshoe map has an invariant set in the square S (cf. Figure 4.1), but again all initial conditions except for a set of Lebesgue measure zero eventually leave the square.[1] The invariant sets for these two cases are examples of nonattracting chaotic sets. While it is clear that chaotic attractors have practically important observable consequences, it may not at this point be clear that nonattracting chaotic sets also have practically important observable consequences. Perhaps the three most prominent consequences of nonattracting chaotic sets are the phenomena of *chaotic transients*, *fractal basin boundaries*, and *chaotic scattering*.

The term chaotic transient refers to the fact that an orbit can spend a long time in the vicinity of a nonattracting chaotic set before it leaves, possibly moving off to some nonchaotic attractor which governs its motion ever after. During the initial phase, when the orbit is in the vicinity of the nonattracting chaotic set, its motion can appear to be very irregular and is, for most purposes, indistinguishable from motion on a chaotic attractor.

Say we sprinkle a large number of initial conditions with a uniform distribution in some phase space region W containing the nonattracting chaotic set. Then the length of the chaotic transient that a given one of these orbits experiences depends on its initial condition. The number $N(\tau)$ of orbits still in the chaotic transient phase of their orbit after a time τ typically decays exponentially with τ, $N(\tau) \sim \exp -(\tau/\langle\tau\rangle)$, for large τ. Thus, the fraction of orbits $P(\tau)\,d\tau$ with chaotic transient lengths between τ and $\tau + d\tau$ is

$$P(\tau) = dN(\tau)/d\tau \sim \exp -(\tau/\langle\tau\rangle), \tag{5.1}$$

where we call $\langle\tau\rangle$ the average lifetime of a chaotic transient. We can also interpret $P(\tau)$ as the probability distribution of τ, given that we choose an initial condition randomly in the region W containing the nonattracting chaotic set. We have already seen examples of the exponential decay law (5.1) for the case of the map Eq. (3.3) and the horseshoe map (cf. Figure 4.1). In particular, referring to Eq. (3.5), we see that, for this example,

$$\langle\tau\rangle = [\ln(1 - \Delta)^{-1}]^{-1},$$

Hence, the average transient lifetime can be long if Δ is small. In such a case observations of an orbit for some appreciable time duration of the order of $\langle\tau\rangle$ or less may not be sufficient to distinguish a chaotic transient from a chaotic attractor.

We shall be discussing chaotic transients in greater detail in Chapter 8 In this chapter we will concentrate on fractal basin boundaries and chaotic scattering. We will also present general results relating the Lyapunov exponents and the average decay time $\langle\tau\rangle$ to the fractal dimensions of nonattracting chaotic sets. (A useful review dealing with some of this material has been written by Tél (1991).)

5.1 Fractal basin boundaries

Dynamical systems can have multiple attractors, and which of these is approached depends on the initial condition of the particular orbit. The closure of the set of initial conditions which approach a given attractor is the basin of attraction for that attractor. From this definition it is clear that the orbit through an initial condition inside a given basin must remain inside that basin. Thus, basins of attraction are invariant sets.

As an example, consider the case of a particle moving in one dimension under the action of friction and the two-well potential $V(x)$ illustrated in Figure 5.1(a). Almost every initial condition comes to rest at one of the

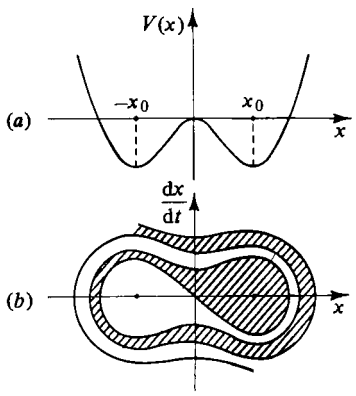

Figure 5.1(a) Potential $V(x)$ for a point particle moving in one dimension. (b) The basins of attraction for the attractors at $x = x_0$ (crosshatched) and at $x = -x_0$ (uncrosshatched).

two stable equilibrium points $x = x_0$ or $x = -x_0$. Figure 5.1(*b*) schematically shows the basins of attraction for these two attractors in the position–velocity phase space of the system. Initial conditions starting in the crosshatched region are attracted to the attractor at $x = +x_0$, $dx/dt = 0$, while initial conditions starting in the uncrosshatched region are attracted to the attractor at $x = -x_0$, $dx/dt = 0$. The boundary separating these two regions (the 'basin boundary') is, in this case, a simple curve. This curve goes through the unstable fixed point $x = 0$. Initial conditions on the basin boundary generate orbits that eventually approach the unstable fixed point $x = 0$, $dx/dt = 0$. Thus, *the basin boundary is the stable manifold of an unstable invariant set*. In this case the unstable invariant set is particularly simple (it is the point $x = 0$, $dx/dt = 0$). We shall see, however, that the above statement also holds when the unstable invariant set is chaotic.

For the example of Figure 5.1 the basin boundary was a simple curve. We now give several pictorial examples showing that basin boundaries can be much more complicated than is the case for Figure 5.1.

Figure 5.2(*a*) shows the basins of attraction for the map (Grebogi *et al.*, 1983a; McDonald *et al.*, 1985),

$$\theta_{n+1} = \theta_n + a \sin 2\theta_n - b \sin 4\theta_n - x_n \sin \theta_n, \tag{5.2a}$$

$$x_{n+1} = -J \cos \theta_n, \tag{5.2b}$$

where $J_0 = 0.3$, $a = 1.32$ and $b = 0.90$. This map has two fixed points, $(\theta, x) = (0, -J_0)$ and (π, J_0), which are attracting. Figure 5.2 was constructed using a 256×256 grid of initial conditions. For each initial condition the map was iterated a large number of times. It was found that all the initial conditions generate orbits which go to one of the two fixed point attractors. Thus, we conclude that these are the only attractors for this map. If an initial condition yields an orbit which goes to $(0, -J_0)$, then a black dot is plotted at the location of the initial condition. If the orbit goes to the other attractor, then no dot is plotted. (The size of the plotted points on the grid is such that, if all points were plotted, the entire region would be black.) Thus, the black and blank regions are essentially pictures of the two basins of attraction to within the accuracy of the grid used. The graininess in this figure is due to the finite resolution used. At any rate it is apparent that very fine-scale structure in the basins of attraction is present. Furthermore, this fine-scale structure is evidently present on all scales, as revealed by examining magnifications of successively smaller and smaller regions of the phase space which contain fine scale structure. Figure 5.2(*b*) shows such a magnification. We see that on a small scale the basins evidently consist of many narrow black and blank parallel strips of varying widths. In fact, as we shall see, the basin

boundary on this scale may be regarded as a Cantor set of parallel lines (separating the black and blank regions), and the fractal dimension of this basin boundary has been numerically computed to be approximately 1.8 (Grebogi *et al.*, 1983a).

Figure 5.3 shows the basin structure for the forced damped pendulum equation

$$d^2\theta/dt^2 + 0.1\, d\theta/dt + \sin\theta = f\cos t$$

for two cases, $f = 1.2$ (Figure 5.3(*a*)) and $f = 2.0$ (Figure 5.3(*b*)) (Grebogi, Ott and Yorke, 1987c). In both cases there are two periodic attractors that have the same period as the forcing (namely 2π). The orbit for one of these two attractors has average clockwise motion (negative average value of $\dot{\theta}$), while the orbit for the other attractor has average counterclockwise motion. In Figure 5.3 the black region represents initial ($t = 0$) values of θ and $\dot{\theta}$ that asymptote to the attractor whose orbit has average counterclockwise motion. Again, we see that there is small scaled structure on which the black and blank regions appear to be finely interwoven. This is again a manifestation of the fractal nature of the basin boundaries. Numerical experiments on the forced damped pendulum

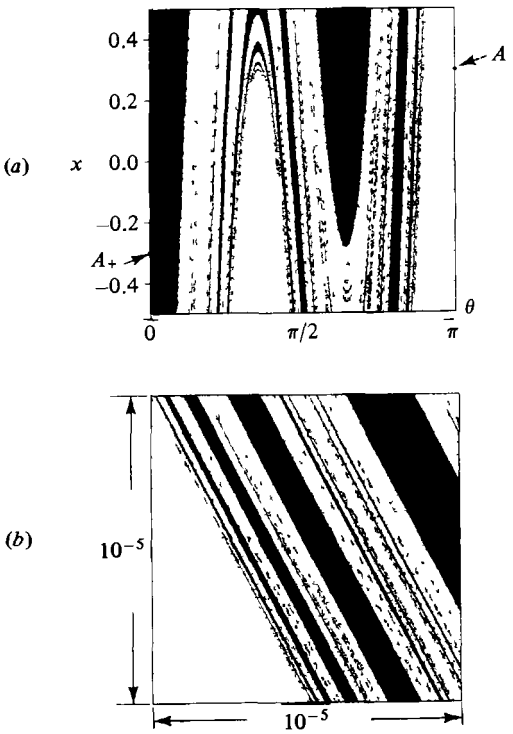

Figure 5.2(*a*) Basins of attraction for Eqs. (5.2). A_+ and A_- denote the two fixed point attractors. (*b*) Magnification by a factor of 10^5 of the region in (*a*) given by $1.92200 \le \theta \le 1.92201$ and $-0.50000 \le x \le -0.49999$ (McDonald *et al.*, 1985).

equation show that fractal basin boundaries are extremely common for this system.

As a further illustrative example, consider the 'kicked double rotor' mechanical system illustrated in Figure 5.4. A fixed pivot is attached to a bar with moment of inertia I_1. The free end of this bar is attached by a pivot to the middle of a second bar of moment of inertia I_2. An impulsive upward vertical force, $F = f\Sigma_n \delta(t - nT)$, is periodically applied to one end of the second bar at time instants $t = 0, T, 2T, 3T, \ldots$. There is friction at the two pivots with coefficients v_1 and v_2. Examining the positions (θ, ϕ) and the angular velocities $(\mathrm{d}\theta/\mathrm{d}t, \mathrm{d}\phi/\mathrm{d}t)$ just after an impulsive kick, we can analytically derive a four-dimensional map giving the positions and angular velocities just after the $(n + 1)$th kick in terms of their values just after the nth kick (Grebogi *et al.*, 1987a). Figure 5.5 shows the basin structure for this map for a particular set of the parameters f, I_1,

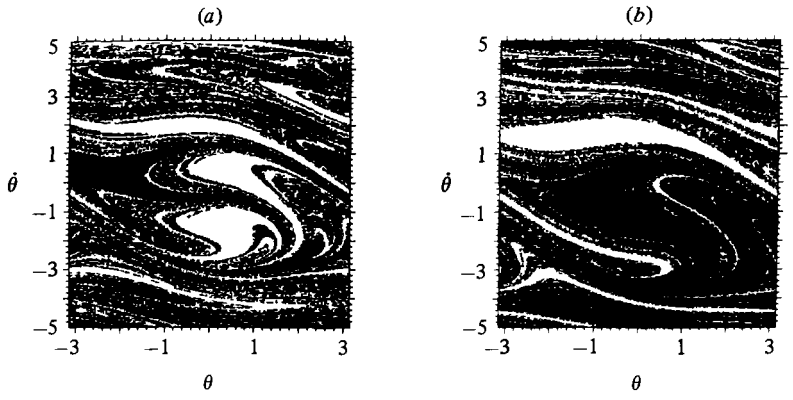

Figure 5.3 Basins of attraction for the forced damped pendulum equation using a grid of over 10^6 initial conditions in each case (Grebogi *et al.*, 1987c).

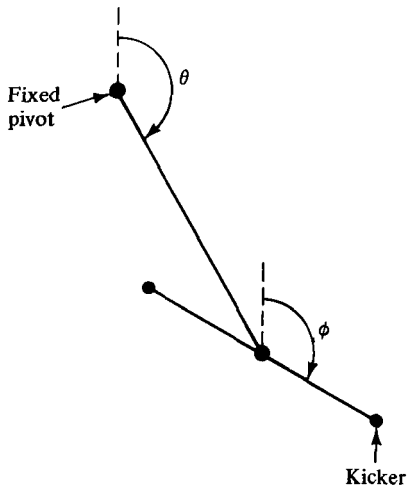

Figure 5.4 The double rotor (there is no gravity).

I_2, ν_1 and ν_2. For this choice of parameters there are two attractors; one is the stable fixed point $\theta = \phi = 0$, $d\theta/dt = d\phi/dt = 0$ (both arms are oriented straight up), while the other attractor is chaotic. The plot in Figure 5.5(*a*) and the magnification in Figure 5.5(*b*) show initial conditions on a two-dimensional surface in the four-dimensional phase space (namely, the surface $d\theta/dt = d\phi/dt = 0$), with the black region corresponding to the basin of the fixed point attractor and the blank region corresponding to the basin of the chaotic attractor. Thus, we can regard Figure 5.5(*a*) as a 'slice' by a two-dimensional plane cutting across the four-dimensional phase space. Numerically, it is found that the boundary between the black and blank regions in Figure 5.5 has dimension 1.9, corresponding to a dimension of the basin boundary in the full four-dimensional phase space[2] of 3.9.

Fractal basin boundaries also occur for one-dimensional maps Consider the map shown in Figure 5.6(*a*), where the map function consists of straight lines in $[0, \frac{1}{5}]$, $[\frac{2}{5}, \frac{3}{5}]$, $[\frac{4}{5}, 1]$. This map has two attracting fixed points, labeled A_+ and A_-. The region $x \geq 1$ is part of the basin of attraction for A_+ and that the region $x \leq 0$ is part of the basin of attraction for A_-. We now focus on the structure of the basins in $[0, 1]$ Since the interval $[\frac{1}{5}, \frac{2}{5}]$ maps to $x \geq 1$, it is in the basin of A_+. Since the interval $[\frac{3}{5}, \frac{4}{5}]$ maps to $x \leq 1$, it is in the basin of A_-. This is indicated in Figure 5.6(*b*). We now ask, which intervals map to $[\frac{1}{5}, \frac{2}{5}]$ and which to $[\frac{3}{5}, \frac{4}{5}]$? These are the six intervals of length $\frac{1}{25}$ shown in Figure 5.6(*b*). We see that, at this stage of the construction, the intervals assigned to the two basins alternate between the basin of A_+ and the basin of A_- as we move from $x = 0$ to $x = 1$. In fact, this is true at every stage of the construction Thus, we build up a very complicated, finely interwoven basin structure, and the boundary between the two basins is the nonattracting invariant

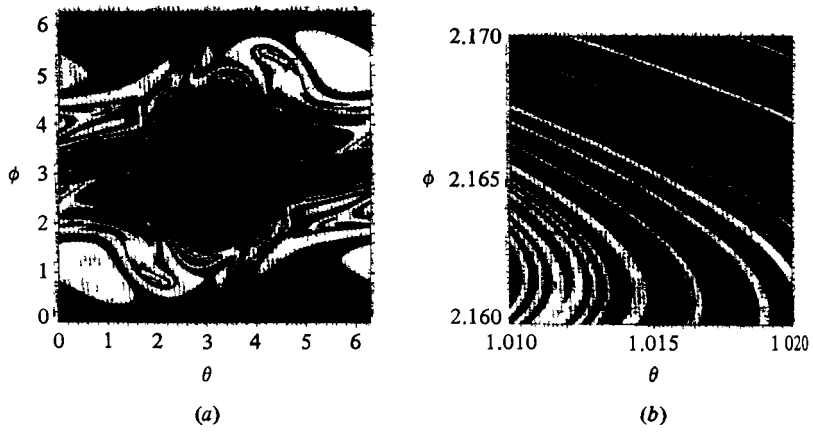

Figure 5.5 Basins of attraction for the kicked double rotor; (*b*) shows a manifestation of a small subregion of (*a*) (Grebogi *et al.*, 1987a).

Cantor set of points which never leave the interval [0, 1]. (The dimension of this Cantor set is (ln 3)/(ln 5).)

As a final example of a fractal basin boundary, consider the logistic map, $x_{n+1} = M(x_n) \equiv rx_n(1 - x_n)$, in the range of r-values for which there is an attracting period three orbit. Although there is only one attractor in this case (the period three orbit), we can create a situation where there are three attractors by considering the map $M^3(x)$ rather than $M(x)$ (see Figure 2.13). In this case there are three fixed point attractors, which are just the three components of the attracting period three orbit of $M(x)$, and the boundary separating their basins is fractal (McDonald *et al.*, 1985; Park *et al.*, 1989; Napiórkowski, 1986). Figure 5.7 shows the basin of the middle fixed point attractor of $M^3(x)$ (blank regions) as a function of r.

For further discussion and examples of fractal basin boundaries see McDonald *et al.* (1985) and the book by Gumowski and Mira (1980).

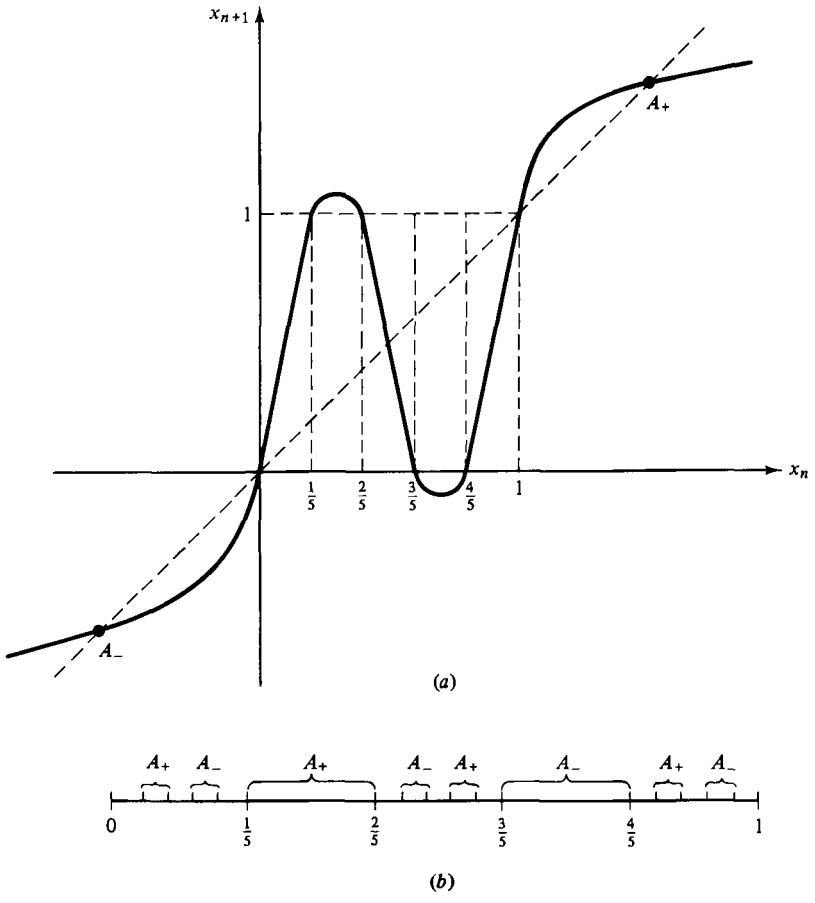

Figure 5.6 (*a*) One-dimensional map with a fractal basin boundary. (*b*) The basin in [0, 1].

5.2 Final state sensitivity

The small scale alternation between different basins that we have seen in the above examples can present a problem when one attempts to predict the future state of a dynamical system. In particular, in the presence of fractal basin boundaries, a small uncertainty in initial conditions can cause anomalously large degradation in one's ability to determine which attractor is approached. In order to make this quantitative, first consider the case of a simple nonfractal basin boundary Σ for two fixed point attractors A_+ and A_-, as shown schematically in Figure 5.8. Say our initial conditions are uncertain by an amount ε in the sense that, when we say that the initial condition is $\mathbf{x} = \mathbf{x}_0$, what we really know is only that the initial condition lies somewhere in $|\mathbf{x} - \mathbf{x}_0| \leq \varepsilon$. For the situation in Figure 5.8, under uncertainty ε, we know for sure that initial condition 1 goes to attractor A_+. On the other hand, the point labeled 2 in the figure lies in the basin of attractor A_-, but because of the ε uncertainty, the actual orbit may go to either attractor A_+ or attractor A_-. We call initial condition 1 ε-certain and initial condition 2 ε-uncertain. Clearly, initial conditions that are ε-uncertain are those which lie within a distance ε of the basin boundary Σ. If we were to pick an initial condition at random in the rectangle shown in Figure 5.8, the probability of obtaining an ε-uncertain initial condition is the fraction of the area (or, in higher dimensionality, volume) of the phase space which lies within ε of the boundary Σ. Denote this fraction $f(\varepsilon)$. For a simple nonfractal boundary, as in Figure 5.8, $f(\varepsilon)$ scales linearly with ε, $f(\varepsilon) \sim \varepsilon$. Thus improvement of the initial condition accuracy say by a factor of 10 (i.e., reduction of ε by 10), reduces $f(\varepsilon)$ and hence our probability of potential error by a factor of 10. However, as we show in the appendix, when the boundary is fractal, $f(\varepsilon)$ has a different scaling with ε;

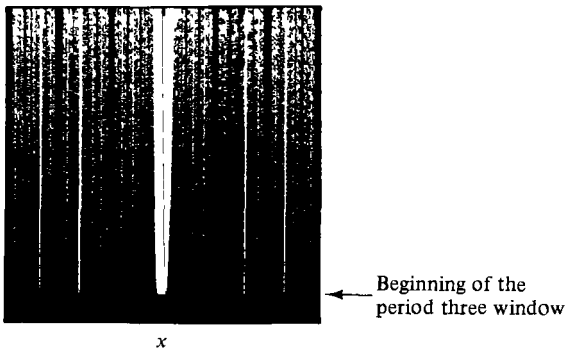

Figure 5.7 Basin structure of the third iterate of the logistic map in the period three window (Park *et al.*, 1989).

$$f(\varepsilon) \sim \varepsilon^{\alpha}, \tag{5.3a}$$

$$\alpha = N - D_0, \tag{5.3b}$$

where N is the phase space dimensionality and D_0 is the box-counting dimension of the basin boundary. For a nonfractal boundary $D_0 = N - 1$ and $\alpha = 1$. For fractal basin boundaries, such as those in Figures 5.2–5.4, $D_0 > N - 1$ and hence $\alpha < 1$. For example, for the situation in Figure 5.5 we have $N = 4$, $D_0 \approx 3.9$, and hence $\alpha = 0.1$. Thus $f(\varepsilon) \sim \varepsilon^{0.1}$. In this case there is relatively little one can do to reduce $f(\varepsilon)$ by improving the accuracy of initial conditions. In the case of Figure 5.5 ($\alpha \approx 0.1$), to reduce $f(\varepsilon)$ by a factor of 10 requires a reduction of ε by a factor of 10^{10}! If $\alpha < 1$ (i.e., the boundary is fractal), then we say there is *final state sensitivity*, and, as the example above makes clear, the situation with respect to potential improvement in prediction by increasing initial condition accuracy is less favorable the smaller α is. (Note in Eq. (5.3b) that the dimension D_0 satisfies $D_0 \geq N - 1$, since the basin boundary must divide the phase space; hence α cannot exceed 1.) We call α the 'uncertainty exponent'.

The dimension of a fractal basin boundary can be numerically calculated on the basis of the above discussion (McDonald *et al.*, 1983). For example, for the case of the basin boundary shown in Figure 5.2 we proceed as follows. Consider an initial condition (θ_0, x_0), and perturb its x coordinate by an amount ε producing two new initial conditions, $(\theta_0, x_0 - \varepsilon)$ and $(\theta_0, x_0 + \varepsilon)$. Now iterate the map and determine which attractor (A_+ or A_-) each of the three initial conditions goes to. If they do not all go to the same attractor, then we count the original initial condition as uncertain. Now, we randomly choose a large number of initial conditions in the rectangle of Figure 5.3. We then determine the fraction $\bar{f}(\varepsilon)$ of these that are uncertain, and we repeat this for several values of ε. From the definitions of $f(\varepsilon)$ and $\bar{f}(\varepsilon)$, we expect that f is approximately proportional to $\bar{f}$ (for further discussion see Grebogi *et al.* (1988a)) so that α can be extracted from the scaling of $\bar{f}$ with ε. Figure 5.9

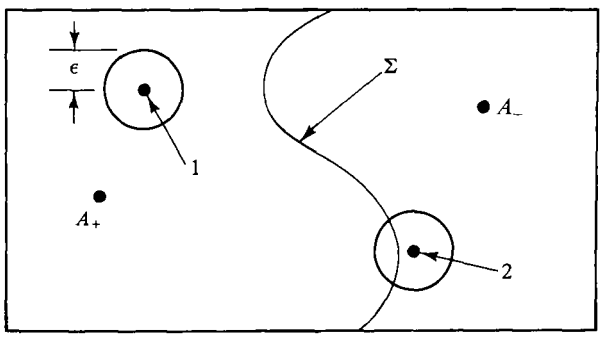

Figure 5.8 Region of phase space divided by a nonfractal basin boundary Σ.

shows results from a set of numerical experiments plotted on log–log axes. The straight line fit indicates that $\bar{f}$ scales as a power of ε, and the slope of the line gives the power α. The result is $\alpha \approx 0.2$, from which Eq. (5.3) yields $D_0 \approx 1.8$.

Even when error in initial conditions is essentially absent, errors in the specification of parameter values specifying the system may be present (e.g., the parameter f in the pendulum equation used in Figure 5.3; $d^2\theta/dt^2 + 0.1\, d\theta/dt + \sin\theta = f\cos t$). A small error in a system parameter might alter the location of the basin boundary so that a fixed initial condition shifts from one basin to another. In a finite region of parameter space, the fraction of randomly chosen parameter values which produces such a change when perturbed by a parameter error δ is some uncertain fraction which we denote $f_p(\delta)$. If the basin boundary dimension is approximately constant in the region of parameter space examined, then the scaling of $f_p(\delta)$ is the same as that for $f(\varepsilon)$; $f_p(\delta) \sim \delta^\alpha$ with

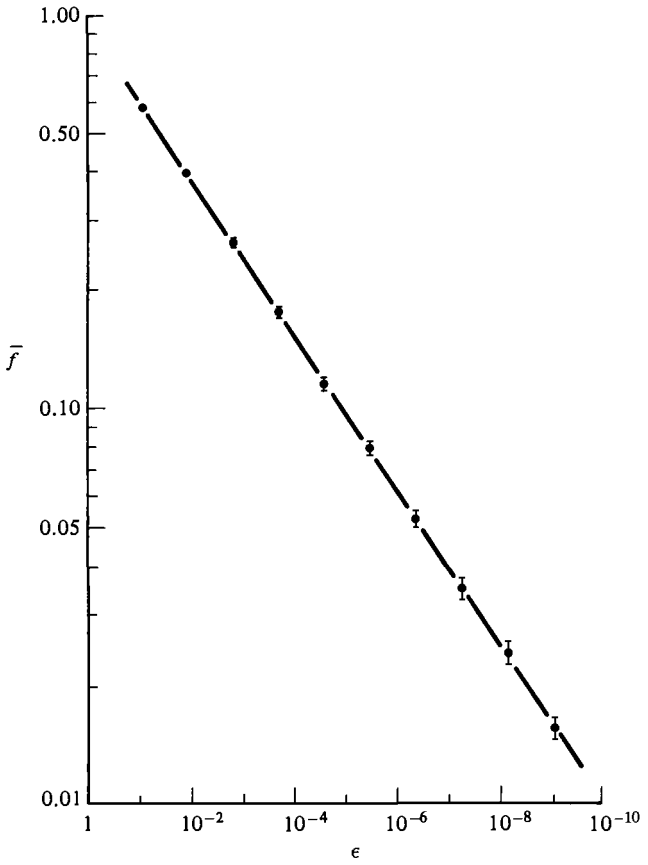

Figure 5.9 $\bar{f}$ versus ε (McDonald *et al.*, 1985).

$\alpha = N - D_0$. Moon (1984) has experimentally examined the parameter dependence of the system in Figure 1.1 to see which attractor a fixed initial condition goes to, and he has concluded, on this basis, that the basin boundary is fractal.

In addition to final state and parameter sensitivity, another practical consequence of fractal basin boundaries and nonattracting chaotic sets has been investigated in the Josephson junction experiments of Iansiti *et al.* (1985). These authors find that, when periodic attractors are near a fractal basin boundary, noise can cause frequent kicks of the orbit into the region of finely interwoven basin structure. This leads to an orbit which resembles a chaotic orbit on a strange attractor even when the noise is relatively small.

5.3 Structure of fractal basin boundaries

We now give a description of how the dynamics of the map Eq. (5.2) leads to the fractal basin boundary structure in Figure 5.2. Figure 5.10(*a*) schematically shows a region of the phase space in $0 \leq \theta \leq \pi$ (and narrower in x than the region shown in Figure 5.2). In addition to the two fixed point attractors A_+ and A_-, there are also three other fixed points which are not attracting. These three, labeled S_+, S_- and S_0, are saddles; that is, they have a one-dimensional stable manifold and a one-dimensional unstable manifold. We are particularly interested in the saddles S_+ and S_- segments of whose stable manifolds *ab* and *cd* are indicated in the figure. The entire region to the left of *ab* (right of *cd*) can be shown to be part of the basin of attraction of the fixed point attractor A_+ (A_-). The question now becomes, what is the basin structure in the region $Q = abcd$ which lies between the two stable manifold segments *ab* and *cd*? (Q is shown crosshatched in Figure 5.10(*a*).) For the purpose of addressing this question, we show an expanded schematic view of the region Q in Figure 5.10(*b*). The action of the map on Q is to take it into the *S*-shaped crosshatched region shown in Figure 5.10(*b*), where the map takes *a* to *a'*, *b* to *b'*, *c* to *c'* and *d* to *d'*. The stable manifold segments *ab* and *cd* divide the S-shaped region $\mathbf{M}(Q)$ into five subregions, labeled I', II', III', IV' and V'. The region II' lies to the right of the stable manifold of S_- and so is in the basin of attraction of A_-. Similarly, region IV' is in the basin of A_+. We now ask, what are the preimages of these regions? In particular, the preimage of II' (which we denote II) will be in the basin of A_-, and the preimage of the region IV' (denoted IV) will be in the basin of A_+. These preimages are shown in Figure 5.11. Since the region $\mathbf{M}(Q) \cap$ II is in the basin of A_- its preimage, $\mathbf{M}^{-1}[\mathbf{M}(Q) \cap \text{II}]$ is also in the basin of A_-. This preimage is also shown in Figure 5.11 as the three narrow crosshatched

vertical strips. Similarly, $\mathbf{M}^{-1}[\mathbf{M}(Q) \cap \mathrm{IV}]$ is the three narrow shaded vertical strips and is part of the basin of A_+. Proceeding iteratively in this way we build up successively finer and finer scale resolution of the basin structure. Note that the shaded and crosshatched vertical strips alternate as we move horizontally across Q, and that this is true at all stages of the construction.[3] Note the similarity of the action of the map on the region Q in Figure 5.10 with the horseshoe map (imagine turning Figure 4.1(d) on its side). The main difference is that $\mathbf{M}(Q) \cap Q$ consists of *three* strips for the case in Figure 5.10, while the action of the horseshoe map on the square produces a region (the horseshoe) which intersects the original square in *two* strips. A symbolic dynamics of the chaotic invariant set for Figure 5.10 can be worked out in analogy to the horseshoe analysis (cf. Problem 1 of Chapter 4), and is a full shift on three symbols (in contrast with the two symbols of the horseshoe map). As in the horseshoe, we may

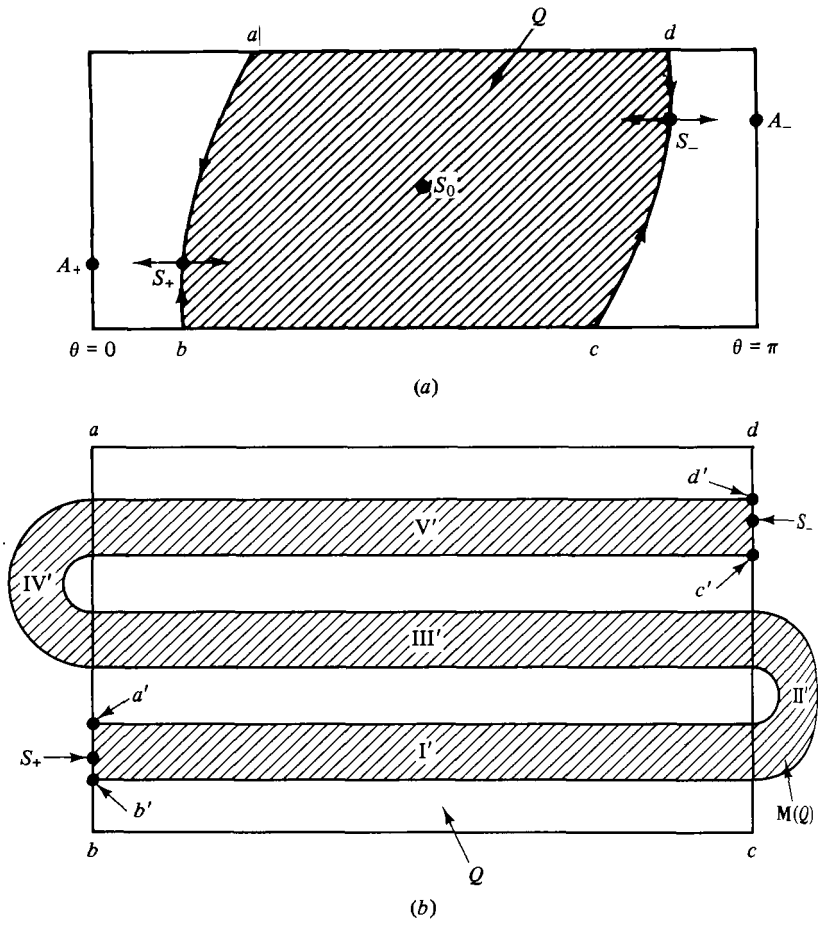

Figure 5.10 Schematic illustration of the construction of the basin structure for the map Eq. (5.2).

think of the chaotic invariant set as the intersection of a Cantor set of lines running vertically with a Cantor set of lines running horizontally. Furthermore, the Cantor set of vertically oriented lines constitutes the basin boundary in the region Q, and is also the stable manifold of the chaotic invariant set. (The horizontal lines are the unstable manifold.) Thus, we see that, in both this example and the example of the two well potential (Figure 5.1), the basin boundary is the stable manifold for a nonattracting invariant set (i.e., the point $x = dx/dt = 0$ for Figure 5.1 and a nonattracting chaotic invariant set for the case of Figure 5.10).

We emphasize that the type of basin structure we have found here, locally consisting of a Cantor set of smooth curves, is very common, but it is not the only type of structure that fractal basin boundaries for typical dynamical systems can have. In particular, McDonald *et al.* (1985) and Grebogi *et al.* (1983b, 1985a) give an example where the basin boundary can be analytically calculated and is a continuous, but nowhere differentiable, curve. The example they consider is the following map,

$$x_{n+1} = \lambda_x x_n \pmod 1, \tag{5.4a}$$

$$y_{n+1} = \lambda_y y_n + \cos(2\pi x_n), \tag{5.4b}$$

with λ_y and λ_x greater than 1 and λ_x an integer greater than λ_y.

This map has no attractors with finited y (cf. Problem 4 of Chapter 4). Almost every initial condition generates an orbit which approaches either $y = +\infty$ or $y = -\infty$. We regard $y = +\infty$ and $y = -\infty$ as the two attractors for this system. The basins of attraction are shown in Figure 5.12 (the $y = -\infty$ attractor is shown black). The analysis shows that the basin boundary is the continuous curve given by

$$y = -\sum_{j=1}^{\infty} \lambda_y^{-1} \cos(2\pi\lambda_x^{j-1} x). \tag{5.5}$$

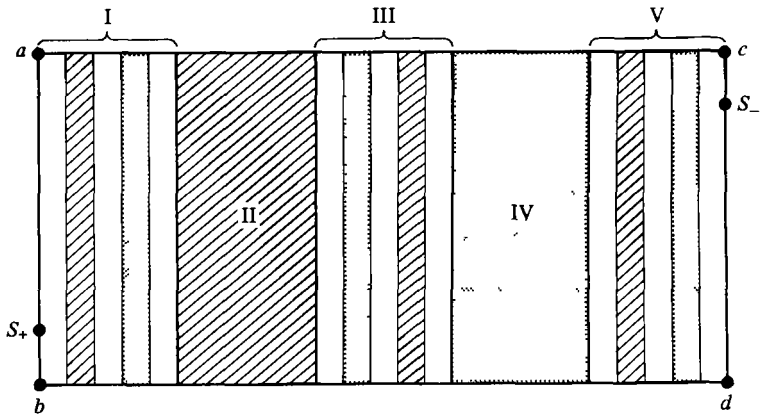

Figure 5 11 The basin of A is shown cross-hatched, and the basin of A_+ is shown shaded

The sum converges since $\lambda_y > 1$. The derivative dy/dx does not exist, however; differentiating inside the sum produces the sum

$$\frac{2\pi}{\lambda_x} \sum_{j=1}^{\infty} \left(\frac{\lambda_x}{\lambda_y}\right)^j \sin(2\pi\lambda_x^{j-1}x),$$

which does not converge since we have assumed $(\lambda_x/\lambda_y) > 1$. Equation (5.5) is called a Weierstrass curve and has fractal dimension

$$D_0 = 2 - [(\ln \lambda_y)/(\ln \lambda_x)]$$

(which is $D_0 = 1.62\ldots$ for the parameters of Figure 5.12).

Another type of basin structure that is common is the case where the same basin boundary can have different dimensions in different regions. Furthermore, in a certain sense, these regions of different dimension can be intertwined on arbitrarily fine scale (Grebogi *et al.*, 1987a). An example illustrating this phenomenon is the basin boundary of the kicked double rotor shown in the cross section in Figure 5.5. In Figure 5.5(*a*) we see that the boundary between the black and blank areas in the region $0 \leq (\theta, \phi) \leq 1$ appears to be a simple smooth curve ($D_0 = 1$) sharply dividing the two basins. On the other hand the very mixed appearance in the central region surrounding the point $\theta = \phi = \pi$ suggests that the boundary is fractal there. Indeed application of the numerical final state sensitivity technique to the region $0 \leq (\theta, \phi) \leq 2\pi$ yields a dimension of the boundary of approximately 1.9 (in the $d\theta/dt = d\phi/dt = 0$ cross section). Note, however, that, when we consider two sets, S_a and S_b, of different dimensions, d_a and d_b, the dimension of the union of the two sets is the larger of the dimensions of the two sets,

$$\dim(S_a \cup S_b) = \max(d_a, d_b).$$

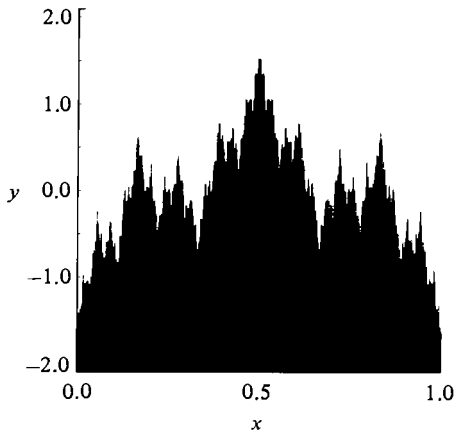

Figure 5.12 Basins for Eqs. (5.4) with $\lambda_z = 3$ and $\lambda_y = 1.5$ (McDonald *et al.*, 1985).

Thus, there is no contradiction with our observation that the dimension in $0 \leq (\theta, \phi) \leq 1$ is 1. (Indeed applying the final state sensitivity technique to the region $0 \leq (\theta, \phi) \leq 1$ yields $D_0 = 1$.) Now, consider the magnification shown in Figure 5.5(*b*). The dimension of the boundary in this small region is again $D_0 \approx 1.9$. Note, however, that there are areas within this small region where the basin boundary is apparently one-dimensional (e.g. $1.010 \leq \theta \leq 1.012$, $2.160 \leq \phi \leq 2.162$). Moreover, this situation is general for the double rotor: Given any square subregion within $0 \leq (\theta, \phi) \leq 2\pi$ which contains part of the basin boundary, the boundary in that square is nonfractal ($D_0 = 1$) or fractal, and if it is fractal its dimension is always the same ($D_0 \approx 1.9$). Furthermore, no matter how small the square is, if the dimension of the boundary in the square is fractal, then there is some smaller square within it for which the contained boundary is not fractal ($D_0 = 1$). Thus, regions of the basin boundary with different dimension are interwoven on arbitrarily fine scale. For further discussion of this phenomenon and how it comes about as a result of the dynamics see Grebogi *et al.* (1987a, 1988a).

So far we have been discussing fractal boundaries that separate the basins of different attractors. We wish to point out, however, that fractal boundaries can also occur even in conservative (nondissipative) systems for which attractors do not exist. As a simple example of this type, consider the motion of a point particle without friction moving along straight line orbit segments in a region bounded by hard walls (shown in Figure 5.13(*a*)) at which the particle experiences specular reflection on each encounter (Bleher *et al.*, 1988). We examine initial conditions on the dashed horizontal line segment shown in Figure 5.13(*a*). The initial position x_0 is measured from the center of the line and the initial velocity

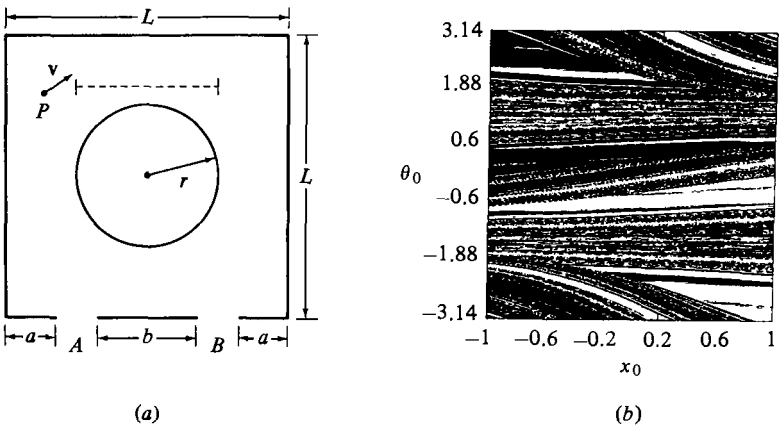

Figure 5.13(*a*) Particle moving in a region with reflecting walls and two holes *A* and *B*. (*b*) Initial conditions in the black region exit through hole *A* ($r = 1$, $L = 4$, $a = 0.1$, $b = 0.2$) (Bleher *et al.*, 1988).

vector angle θ_0 is measured clockwise from the vertical. Figure 5.13(*b*) shows the regions of this initial condition space for which the particle exits through hole A (black) and for which it exits through hole B (blank). The dimension of the boundary separating these two regions is numerically found to be approximately 1.8. Blow-ups, however, reveal that there is the same sort of fine-scaled interweaving of fractal ($D_0 \approx 1.8$) and nonfractal ($D_0 = 1$) boundary regions as for the kicked double rotor example.

5.4 Chaotic scattering

In this section we consider the classical scattering problem for a conservative dynamical system.[4] The simplest example of this problem deals with the motion without friction of a point particle in a potential $V(\mathbf{x})$ for which $V(\mathbf{x})$ is zero, or else very small, outside of some finite region of space which we call the scattering region. Thus, the particle moves along a straight line (or an approximately straight line) sufficiently far outside the scattering region. We envision that a particle moves toward the scattering region from outside it, interacts with the scatterer, and then leaves the scattering region. The question to be addressed is how does the motion far from the scatterer after scattering depend on the motion far from the scatterer before scattering? As an example, consider Figure 5.14 which shows a scattering problem in two dimensions. The incident particle has a velocity parallel to the x-axis at a vertical displacement $y = b$. After interacting with the scatterer, the particle moves off to infinity with its velocity vector making an angle ϕ to the x-axis. We refer to the quantities b and ϕ as the impact parameter and the scattering angle, and we wish to investigate the character of the functional dependence of ϕ on b.

As an example consider the potential (Bleher *et al.*, 1990)

$$V(x, y) = x^2y^2 \exp[-(x^2 + y^2)] \tag{5.6}$$

shown in Figure 5.15. This potential consists of four potential 'hills' with equal maxima at (x, y)-coordinate locations $(1, 1)$, $(1, -1)$, $(-1, 1)$, and $(-1, -1)$. The maximum value of the potential is $E_m = 1/e^2$. For large distances $r = (x^2 + y^2)^{1/2}$ from the origin, $V(x, y)$ approaches zero rapidly with increasing r. Figure 5.16(*a*) shows a plot of the *scattering function*, ϕ versus b, for the case where the incident particle energy E is larger than E_m. We observe for this case ($E/E_m = 1.626$) that the scattering function is a smooth curve. Furthermore, it is also found to be a smooth curve for all $E > E_m$. Figure 5.16(*b*) shows the scattering function for a case where $E < E_m$. We observe that the numerically computed dependence of ϕ on b is poorly resolved in the regions $0.6 \gtrsim \pm b \gtrsim 0.2$. To